Acoustic Source Estimation with Doppler Processing

Richard J. Kozick
Bucknell University
Department of Electrical Engineering
Lewisburg, PA 17837

Brian M. Sadler
Army Research Laboratory
AMSRL-CI-CN
2800 Powder Mill Road
Adelphi, MD 20783

Abstract

A statistical analysis of differential Doppler estimation is presented that includes the particular features found in aeroacoustic signals from ground vehicles, namely a sum-of-harmonics signal that is randomly scattered by the atmosphere. We use a physics-based statistical model for the scattering to derive the Cramér-Rao bound (CRB) on differential Doppler estimation as a function of the atmospheric conditions, the frequency of the source, and the range of the source. We evaluate the CRB for several cases of interest, and we compare the performance of algorithms with the CRB. We show with measured aeroacoustic data that differential Doppler can be estimated with accuracy that is comparable to the CRB.

1 Introduction

The data collected by a network of aeroacoustic and seismic sensors may be processed to localize the positions of ground vehicles, track the vehicles as they move, and identify the type of vehicle. However, this processing is challenging because sound signals that propagate through the air are scattered by turbulence, causing random fluctuations in the measured data [1]–[8].

In past work [9], we have studied time-delay estimation with widely-separated aeroacoustic sensors. However, accurate time-delay estimates are difficult to obtain for two reasons: the sounds emitted by many ground vehicles have a sum-of-harmonics structure with small time-bandwidth product, and the scattering causes a loss in signal coherence at the sensors. In this paper, we study Doppler estimation for moving sources, and we show that Doppler estimation does not suffer from the difficulties of time-delay estimation. Indeed, the narrowband, harmonic structure of the sources is advantageous for Doppler estimation, and the differential Doppler between two sensors can be estimated *noncoherently* by examining the peaks in the power spectrum at each sensor. We provide a statistical performance analysis of differential Doppler estimation using the scattering propagation model summarized in [8]. Our analysis provides Cramér-Rao bounds (CRBs) on the accuracy of differential Doppler estimation as a function of signal-to-noise ratio (SNR), meteorological conditions, frequency of the source, and the range of the source. We compare the performance of frequency estimation algorithms with the CRB, and we show with measured aeroacoustic data that differential Doppler can be estimated with accuracy that is comparable to the CRB.

The Doppler estimates from sensor nodes may be combined with bearing estimates to improve the localization accuracy of a tracking algorithm. The Doppler estimates also may be used by a

tracking algorithm to improve the accuracy of "data association" between bearings and sources when multiple sources are present. The results presented here can be extended to CRB analysis of source localization with bearing and/or differential Doppler estimates. The path of a moving source may be estimated solely with differential Doppler estimates if five or more sensors are available [10], or differential Doppler may be used in conjunction with bearing estimates.

This paper is organized as follows. The models for the source (sum of harmonics) and the atmospheric scattering are presented in Section 2. The CRBs for differential Doppler estimation are presented in Section 3, along with two algorithms for frequency estimation with scattered signals. Numerical evaluations of the CRBs and computer simulations of frequency estimation with scattered signals are also included in Section 3. Section 4 contains additional examples of Doppler estimation, including differential Doppler estimation using measured aeroacoustic data. Section 5 contains concluding remarks.

2 Models for Source Signals and Propagation

In this section, we present a general model for the signals received by a network of aeroacoustic sensors. We begin by briefly considering models for the signals emitted by ground vehicles and aircraft. Then we develop the model for the scattering caused by atmospheric turbulence for a moving source emitting a single tone. The model is extended to moving sources that emit a sum of harmonics by assuming that the scattering in each harmonic is independent. The scattering model was developed by Wilson, Collier, and others [1]–[7]. The book chapter [8] presents the scattering model for a nonmoving source and discusses the implications for signal processing. We will use the scattering formulation from [8] in this paper, so the reader may refer to [8] for more details.

2.1 Source signals

The typical source of interest has a primary contribution due to rotating machinery (engines), and may include tire and/or exhaust noise, vibrating surfaces, and other contributions. Internal combustion engines typically exhibit a strong sum of harmonics acoustic signature tied to the cylinder firing rate. Tracked vehicles also exhibit tread slap, which can produce very strong spectral lines, while helicopters produce strong harmonic sets related to the blade rotation rates. Turbine engines, on the other hand, exhibit a broader spectrum and consequently call for different algorithmic approaches in some cases. Our focus in this paper is on differential Doppler estimation for sources with harmonic spectra.

2.2 Overview of propagation phenomena

Four phenomena are primarily responsible for modifying a sinusoidal signal emitted by a nonmoving source to produce the signal observed at the sensor network:

1. Transmission loss caused by spreading of the wavefronts, refraction by wind and temperature gradients, ground interactions, and molecular absorption of sound energy.

2. The propagation delay from the source to the sensors.

3. Additive noise at the sensors caused by thermal noise, wind noise, and directional interference.

4. Random fluctuations in the amplitude and phase of the signals caused by scattering from random inhomogeneities in the atmosphere such as turbulence.

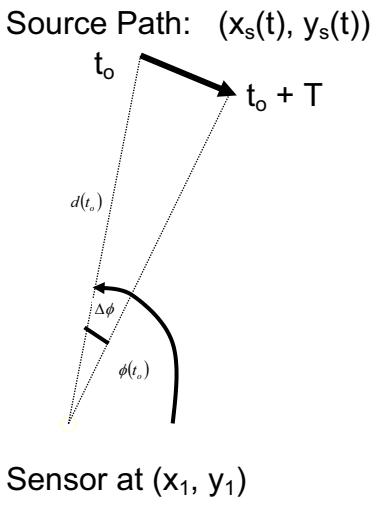

Figure 1: Geometry of one sensor and a source moving in a straight line at constant velocity.

The transmission loss (TL) is defined as the diminishment in sound energy from a reference value S_{ref}, which would hypothetically be observed in free space at 1 m from the source, to the actual energy observed at the sensor S. To a first approximation, the sound energy spreads spherically; that is, it diminishes as the inverse of the squared distance from the source. In actuality the TL for sound wave propagating near the ground involves many complex, interacting phenomena, so that the spherical spreading condition is rarely observed in practice, except perhaps within the first 10 to 30 m [13]. Several well refined and accurate numerical procedures for calculating TL have been developed [14]. For simplicity, here we model S as a deterministic parameter, which is reasonable when the state of the atmosphere does not change dramatically during the data collection.

The propagation delay is developed using the geometry in Figure 1, where the sensor is located at (x_1, y_1) and the source path is modeled as a straight line with constant velocity over an interval of length T,

$$x_s(t) = x_{s,0} + \dot{x}_s \cdot (t - t_0), \quad t_0 \le t \le t_0 + T \tag{1}$$

$$y_s(t) = y_{s,0} + \dot{y}_s \cdot (t - t_0), \tag{2}$$

where $\dot{x}_s, \dot{y}_s$ are the velocity components. If $d(t)$ is the distance between the source position and the sensor at time t, then the propagation time is well-approximated by [11]

$$\tau(t) = \frac{d(t)}{c} \approx \tau(t_o) + \frac{1}{c} v_r(t_o)(t - t_o) \quad \text{for } \Delta\phi \le 18^\circ, \tag{3}$$

where $\Delta\phi$ is the change in bearing over the observation interval, as shown in Figure 1. In (3), c is the speed of sound and $v_r(t_o)$ is the radial component of the velocity at the start of the observation interval,

$$v_r(t_o) = \frac{x_{s,o} - x_1}{d(t_o)} \dot{x}_s + \frac{y_{s,o} - y_1}{d(t_o)} \dot{y}_s = \dot{x}_s \cos\phi(t_o) + \dot{y}_s \sin\phi(t_o). \tag{4}$$

Thermal noise at the sensors is typically independent from sensor to sensor. In contrast, interference from an undesired source produces additive noise that is (spatially) correlated from sensor to sensor. Wind noise exhibits high spatial correlation over distances of several meters [12]. In this paper, we model the additive noise as independent from sensor to sensor.

Scattering of the signal by turbulence, which is the fourth phenomenon in the preceding list, is particularly significant. The turbulence consists of random atmospheric motions occurring on time scales from seconds to several minutes. Scattering from these motions causes random fluctuations in the complex signals at the individual sensors and diminishes the cross coherence of signals between sensors. The effects of scattering on differential Doppler estimation will be analyzed in Section 3 using the model presented in this section.

2.3 Scattering model for a narrowband, moving source

We now develop the model for the sensor signals incorporating the four phenomena described in the preceding subsection. We assume that the source and the sensor network are in the same plane, and we define (x_m, y_m) for $m = 1, \ldots, M$ as the locations of M sensors. We develop the model for a single sensor at (x_1, y_1), and the extension to M sensors follows easily because the scattering and noise are independent at distinct sensors.

The sinusoidal source signal that is measured at the reference distance of 1 m from the source (without motion) is written

$$s_{\text{ref}}(t) = \sqrt{S_{\text{ref}}} \cos(2\pi f_o t + \chi), \tag{5}$$

where the frequency of the tone is $f_o = \omega_o/(2\pi)$ Hz, the period is T_o sec, the phase is χ, and the amplitude is $\sqrt{S_{\text{ref}}}$. The sound waves propagate with wavelength $\lambda = c/f_o$, and the wavenumber is $k = 2\pi/\lambda = \omega_o/c$. We will represent sinusoidal and narrowband signals by their complex envelope, which is defined as

$$\mathcal{C}\{s_{\text{ref}}(t)\} = \widetilde{s}_{\text{ref}}(t) = s_{\text{ref}}^{(\text{I})}(t) + j\, s_{\text{ref}}^{(\text{Q})}(t) = \left[s_{\text{ref}}(t) + j\, \mathcal{H}\left\{s_{\text{ref}}(t)\right\}\right] \exp\left(-j2\pi f_o t\right) \tag{6}$$

$$= \sqrt{S_{\text{ref}}} \exp\left(j\chi\right). \tag{7}$$

We will represent the complex envelope of a quantity with the notation $\mathcal{C}\{\cdot\}$ or $\widetilde{(\cdot)}$, the in-phase component with $(\cdot)^{(\text{I})}$, the quadrature component with $(\cdot)^{(\text{Q})}$, and the Hilbert transform with $\mathcal{H}\{\cdot\}$. The fast Fourier transform (FFT) is often used to approximate the processing in (7) for a finite block of data, where the real and imaginary parts of the FFT coefficient at frequency f_o are proportional to the I and Q components, respectively. The complex envelope of the sinusoid in (5) is given by (7), which is not time-varying, so the average power is $|\widetilde{s}_{\text{ref}}(t)|^2 = S_{\text{ref}}$.

In the absence of scattering, the model for the signal at the sensor that includes transmission loss, propagation delay (for a moving source), and additive noise is

$$z(t) = s\left[t - \tau(t)\right] \; + \; w(t) \tag{8}$$

$$s(t) = \sqrt{S}\, \cos\left(2\pi f_o t + \chi\right) \tag{9}$$

$$\tau(t) = \tau(t_o) + \frac{1}{c} v_r(t_o)(t - t_o). \tag{10}$$

Combining (9) and (10) into (8) yields the following model for the complex amplitude of the sensor signal in the absence of scattering:

$$\widetilde{z}(t) = \sqrt{S}\, \exp\left\{j\, \left[\chi - 2\pi f_o \tau(t_o)\right]\right\} \exp\left\{-j2\pi \frac{v_r(t_o)}{c} f_o (t - t_o)\right\} \; + \; \widetilde{w}(t) \tag{11}$$

$$= \sqrt{S}\, \exp\left[j\theta\right] \exp\left[-j2\pi f_d (t - t_o)\right] \; + \; \widetilde{w}(t), \tag{12}$$

$$\theta = \chi - 2\pi f_o \tau(t_o), \tag{13}$$

$$f_d = \frac{v_r(t_o)}{c} f_o = \text{Doppler frequency shift.} \tag{14}$$

Thus with no scattering, the complex amplitude in (12) is a pure sinusoid in additive noise. The sinusoidal amplitude $\sqrt{S}$ is determined by the source strength and transmission loss, the phase θ in (13) is determined by the source phase and the propagation time, and the frequency $-f_d$ is the Doppler frequency shift. Note that f_d in (14) is proportional to the source frequency f_o and radial velocity $v_r(t_o)$.

The additive noise $w(t)$ in (8) is a white, Gaussian noise (AWGN) process that is real-valued, continuous-time, and zero-mean with power spectral density (PSD) $G_w(f) = (\mathcal{N}_o/2)$ W/Hz. Therefore the complex envelope $\widetilde{w}(t)$ in (12) is a complex, circular, Gaussian random process with zero mean and PSD $G_{\tilde{w}}(f) = 2\mathcal{N}_o$. The noise moments are then

$$E\{\widetilde{w}(t)\} = 0, \quad -\infty < t < \infty, \tag{15}$$

$$r_{\widetilde{w}}(\xi) = E\{w(t+\xi)w^*(t)\} = 2\mathcal{N}_o\,\delta(\xi) \tag{16}$$

where $E\{\cdot\}$ denotes expectation and $\delta(\xi)$ is the Dirac delta function.

The scattering by atmospheric turbulence introduces random fluctuations in the signals and diminishes the cross coherence between signals at different sensors. Several assumptions and simplifications are involved in the scattering formulation [1]–[7], including that the propagation is line-of-sight (no multipath), and the random fluctuations caused by scattering are complex, circular, Gaussian random processes.

The line-of-sight propagation assumption is reasonable for propagation over fairly flat, open terrain in the frequency range of interest here (below several hundred Hz). Modeling the scattered signals as complex, circular, Gaussian random processes is a substantial improvement on the constant signal model in (12), but it is, nonetheless, rather idealized. Waves that have propagated through a random medium can exhibit a variety of statistical behaviors. Experimental studies [15, 16, 17] conducted over short horizontal propagation distances with frequencies below 1000 Hz demonstrate that the effect of turbulence is highly significant, with phase variations much larger than 2π rad and deep fades in amplitude often developing. The measurements demonstrate that the Gaussian model is valid in many conditions, although non-Gaussian scattering characterized by large phase but small amplitude variations is observed at some frequencies and propagation distances. The Gaussian model applies in many cases of interest, and we apply it in this paper.

The scattering modifies the complex envelope of the signal at the sensor by spreading a portion of the power from the (deterministic) mean component into a zero-mean random process. We denote the scattered process by $\widetilde{v}(t)$, which is a complex, circular, Gaussian random process with zero mean and PSD $G_{\tilde{v}}(f)$. We model $G_{\tilde{v}}(f)$ as a symmetric function centered at 0 Hz with bandwidth B_v Hz. Note that this implies that the autocorrelation function of the scattered process, $r_{\tilde{v}}(\xi)$, is real-valued with coherence time on the order of $1/B_v$ sec. The *saturation* parameter [6, 7], denoted by $\Omega \in [0, 1]$, defines the fraction of average signal power that is scattered from the mean into the random component. The scattering may be *weak* ($\Omega \approx 0$) or *strong* ($\Omega \approx 1$), which are analogous to Rician and Rayleigh fading in the radio propagation literature. The modification of (12) to include scattering is as follows:

$$\begin{aligned}\widetilde{z}(t) &= \widetilde{s}\,[t - \tau(t)] \;+\; \widetilde{w}(t) \\ &= \sqrt{(1-\Omega)S}\,\exp[j\theta]\,\exp[-j2\pi f_d(t-t_o)] \\ &\qquad +\; \sqrt{\Omega S}\,\widetilde{v}(t)\,\exp[j\theta]\,\exp[-j2\pi f_d(t-t_o)] \;+\; \widetilde{w}(t).\end{aligned} \tag{17}$$

In order to satisfy conservation of energy at the sensor with $E\{|\widetilde{s}(t)|^2\} = S$, the scattered process is normalized so that its average power is unity,

$$E\{|\widetilde{v}(t)|^2\} = r_{\tilde{v}}(0) = \int_{-\infty}^{\infty} G_{\tilde{v}}(f)\,df = 1. \tag{18}$$

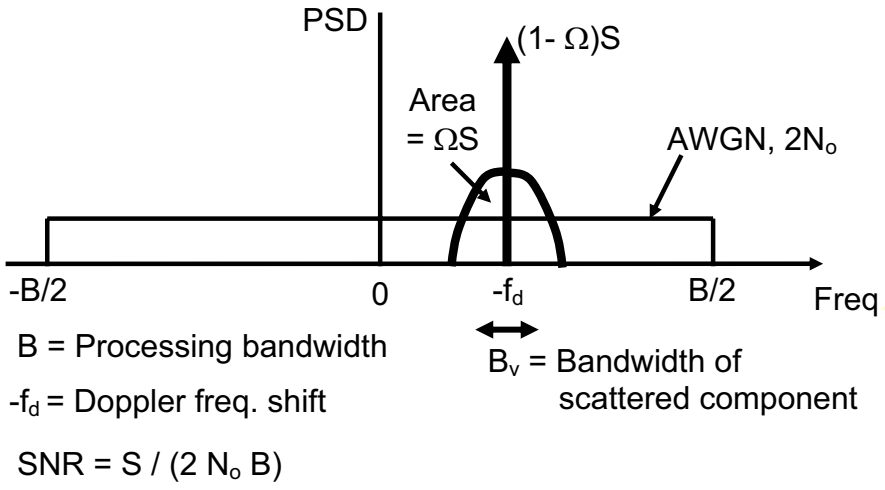

Figure 2: PSD $G_{\tilde{z}}(f)$ for the sensor signal model in (17) for processing bandwidth B Hz.

The PSD $G_{\tilde{z}}(f)$ corresponding to the sensor signal model in (17) is illustrated in Figure 2, and the corresponding formula is

$$G_{\tilde{z}}(f) = (1-\Omega)S\,\delta(f+f_d) \,+\, (\Omega S)\,G_{\tilde{v}}(f+f_d) \,+\, G_{\tilde{w}}(f). \tag{19}$$

The observations are band-pass filtered with bandwidth B Hz, so the AWGN PSD is $G_{\tilde{w}}(f) = 2\mathcal{N}_o\,\mathrm{rect}(f/B)$, where B must be larger than the maximum Doppler frequency shift for the source of interest. The average SNR $= S/(2\mathcal{N}_o B)$. Our objective in this paper is to study algorithms and performance bounds for estimating f_d in Figure 2 as a function of the saturation Ω, the processing bandwidth B Hz, the observation time T sec, the average SNR $= S/(2\mathcal{N}_o B)$, and the bandwidth of the scattered signal B_v. Scattering ($\Omega > 0$) causes fluctuations in the signal energy, with coherence time of the fluctuations proportional to $1/B_v$.

The sensor signals in (17) with PSD in Figure 2 may be sampled at the rate $F_s = B$ samples per second, so the spacing between samples is $T_s = 1/B$. In the observation time of T sec, $N = \lfloor BT \rfloor$ samples are obtained, which are collected in the vector

$$\widetilde{\mathbf{z}} = \begin{bmatrix} \widetilde{z}(0) \\ \vdots \\ \widetilde{z}((N-1)T_s) \end{bmatrix}. \tag{20}$$

This vector has a complex Gaussian distribution with mean and covariance matrix

$$\widetilde{\mathbf{z}} \;\sim\; CN\left(e^{j\theta}\sqrt{(1-\Omega)S}\,\mathbf{a},\; (\Omega\,S)\,\mathbf{R}_{\tilde{v}} \circ \left(\mathbf{a}\mathbf{a}^H\right) \,+\, (2\mathcal{N}_o B)\mathbf{I}\right), \tag{21}$$

where

$$\mathbf{a} = \begin{bmatrix} 1 \\ \exp\left[-j2\pi f_d/B\right] \\ \vdots \\ \exp\left[-j2\pi(N-1)f_d/B\right] \end{bmatrix}, \tag{22}$$

$\mathbf{R}_{\tilde{v}}$ is the covariance matrix of the samples of the scattered process with elements $[\mathbf{R}_{\tilde{v}}]_{mn} = r_{\tilde{v}}\left[(m-n)/B\right]$, $\circ$ denotes element-wise product, $(\cdot)^H$ denotes Hermitian transpose, and $\mathbf{I}$ is the identity matrix.

As noted above, scattering causes fluctuations in the signal energy measured at the sensor. Figure 3(a) shows plots of the probability density function (PDF) of $10\log_{10}|\widetilde{z}(t)|^2$. Note that a small deviation of the saturation from $\Omega = 0$ causes the PDF to spread over several dB. For $\Omega > 0.5$, deviations of 10 to 15 dB are not uncommon. The variation of Ω with source frequency, range, and meteorological condition is discussed in the next subsection.

This model is easily extended to M sensors. The scattered processes at different sensors are independent if the distance between the sensors is larger than a few 10's of m [8]. Thus independent scattering is a reasonable assumption since our focus is on differential Doppler estimation with widely separated sensors.[1] For M sensors, there are distinct Doppler shifts $f_{d,1}, \ldots, f_{d,M}$ and distinct saturation values $\Omega_1, \ldots, \Omega_M$. The scattered processes $\widetilde{v}_1(t), \ldots, \widetilde{v}_M(t)$ are modeled as zero-mean, jointly wide-sense stationary, complex, circular Gaussian random processes that are independent of the noise processes, $E\{\widetilde{v}_n(t+\xi)\widetilde{w}_m(t)^*\} = 0$. The scattered processes are characterized by the autocorrelation function $r_{\tilde{v}}(\xi) = E\{\widetilde{v}_n(t+\xi)\widetilde{v}_n(t)^*\}$, which is assumed to be real-valued and identical for all sensors, with corresponding PSD $G_{\tilde{v}}(f) = \mathcal{F}\{r_{\tilde{v}}(\xi)\}$.

2.4 Model for the saturation

The value of the saturation Ω at a sensor depends on the source distance (d), the source frequency (f_o), and the meteorological conditions. The saturation Ω depends on the source range, d, according to [8]

$$\Omega = 1 - \exp\left(-2\,\mu\,d\right), \tag{23}$$

where μ is called the extinction coefficient for the first moment. An approximate expression for μ as a function of frequency and meteorological condition is [8]

$$\mu \approx \begin{cases} 4.03 \times 10^{-7}\, f_o^2, & \text{mostly sunny conditions} \\ 1.42 \times 10^{-7}\, f_o^2, & \text{mostly cloudy condtions} \end{cases}, \quad f_o \in [30, 200] \text{ Hz}. \tag{24}$$

Figure 3(b) contains a contour plot of (24) for mostly sunny conditions. Note that Ω values over the entire range from 0 to 1 may be encountered for frequencies and source ranges that are typical in aeroacoustics. The saturation varies significantly with frequency for ranges larger than 100 m.

3 Cramér-Rao Bounds and Doppler Frequency Estimation

The CRB provides a lower bound on the variance of any unbiased estimate $\hat{f}_d$, so $E\{|\hat{f}_d - f_d|^2\} \geq \text{CRB}(\hat{f}_d)$. The CRB for the complex Gaussian model in (21) is [20]

$$\text{CRB}(\hat{f}_d) = \text{tr}\left[\mathbf{R}_{\tilde{z}}^{-1}\,\frac{d\,\mathbf{R}_{\tilde{z}}}{d\,f_d}\,\mathbf{R}_{\tilde{z}}^{-1}\,\frac{d\,\mathbf{R}_{\tilde{z}}}{d\,f_d}\right] \;+\; 2\cdot\text{Re}\left[\frac{d\,\mathbf{m}_{\tilde{z}}}{d\,f_d}^H\,\mathbf{R}_{\tilde{z}}^{-1}\,\frac{d\,\mathbf{m}_{\tilde{z}}}{d\,f_d}\right], \tag{25}$$

where $\mathbf{m}_{\tilde{z}} = e^{j\theta}\sqrt{(1-\Omega)}\,\mathbf{a}$, $\mathbf{R}_{\tilde{z}} = \Omega\,\mathbf{R}_{\tilde{v}} \circ \left(\mathbf{a}\mathbf{a}^H\right) + \text{SNR}^{-1}\,\mathbf{I}$, and $\text{tr}(\cdot)$ denotes the trace of a matrix. The derivatives are easily evaluated analytically and the CRB in (25) is evaluated numerically.

Schultheiss and Weinstein [10] derived closed-form expressions for the CRBs when $\Omega = 0$ (no scattering) and $\Omega = 1$ (full scattering). These special cases are illustrated in the PSD plots in

[1] Models are available for the correlation of the scattered processes when the sensors are closely spaced [8].

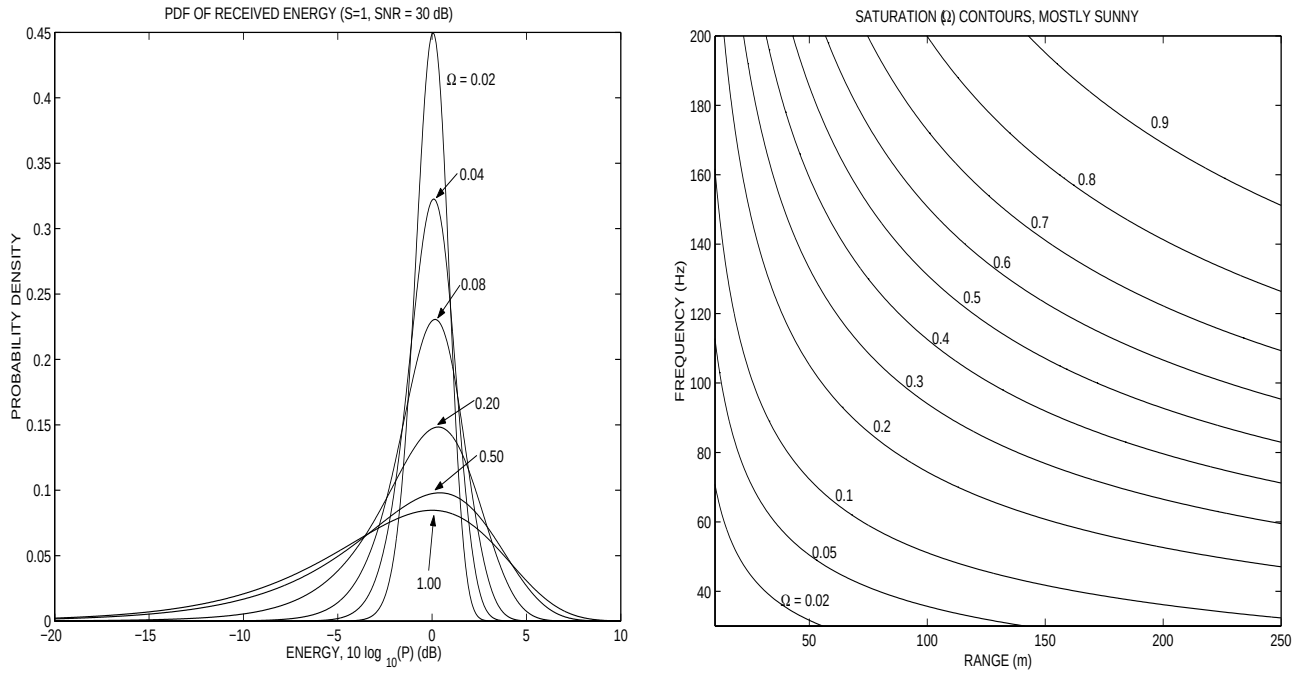

(a) (b)

Figure 3: (a) Probability density function (pdf) of average power measured at the sensor for a signal with average SNR = 30 dB for various values of the saturation, Ω. (b) Variation of saturation Ω with source frequency and range under mostly sunny conditions.

Figure 4, and the CRB expressions from [10] are

$$\Omega = 0: \quad \mathrm{CRB}(\hat{f}_d) = \frac{3}{2\pi^2 T^3}\frac{\mathcal{N}_o}{S} \tag{26}$$

$$\Omega = 1: \quad \mathrm{CRB}(\hat{f}_d) \approx \frac{B_v}{T}\left[\int_0^\infty \left(\frac{d}{dx}\log G_1(x)\right)^2 dx\right]^{-1}. \tag{27}$$

For $\Omega = 1$, the approximation is accurate for high SNR $= S/(2\mathcal{N}_o B)$ and large $B_v T$ = time-bandwidth product of the scattered process. The function $G_1(x)$ in (27) is a normalized form of the scattered PSD with unit bandwidth, so that $G_{\tilde{v}}(f) = (1/B_v)\, G_1(f/B_v)$. Thus with no scattering ($\Omega = 0$), the CRB for frequency estimation gets smaller with higher SNR and longer observation time, T. For full scattering ($\Omega = 1$), the CRB gets smaller with less scattering bandwidth B_v and longer observation time. The CRB for this case also depends on the shape of the scattered PSD through $G_1(x)$.

3.1 Numerical evaluation of CRBs

Next we evaluate the CRBs on frequency estimation as a function of the saturation Ω, the scattering bandwidth B_v, the observation time T, and the average SNR for several cases of interest. We use the following form for the PSD of the scattered signal,

$$G_{\tilde{v}}(f) = \frac{\beta}{B_v}\mathrm{tri}\left(\frac{f}{B_v}\right) + \frac{1-\beta}{B}\mathrm{rect}\left(\frac{f}{B}\right), \tag{28}$$

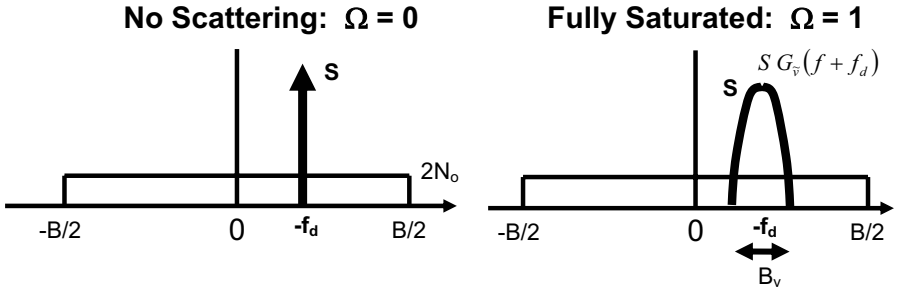

Figure 4: Illustration of the sensor signal PSD for the cases of no scattering ($\Omega = 0$) and full scattering ($\Omega = 1$).

where $\mathrm{tri}(x) = 1 - |x|$ for $|x| \leq 1$ and 0 otherwise, $\mathrm{rect}(x) = 1$ for $|x| \leq 0.5$ and 0 otherwise, and $\beta \in [0, 1]$ determines the fraction of energy in the "peaked" triangular function that has bandwidth B_v. The broader, rectangular component is added to (28) in order to prevent the PSD from reaching the value of 0, which leads to optimistic CRBs. For example, the CRB formula in (27) equals 0 if $G_{\tilde{v}}(f) = 0$ over a frequency interval. We use $\beta = 0.95$ in all of the examples. The effective bandwidth of the scattered signal is approximately $\beta B_v + (1-\beta)B$, and the autocorrelation function of the scattered process is

$$r_{\tilde{v}}(\xi) = \beta \,\mathrm{sinc}^2(B_v \xi) \,+\, (1 - \beta)\,\mathrm{sinc}(B\xi), \tag{29}$$

where $\mathrm{sinc}(x) = \sin(\pi x)/(\pi x)$. The covariance matrix of the scattered samples, $\mathbf{R}_{\tilde{v}}$ in (21), is obtained from (29). The PSD shape-related factor in (27) can be evaluated in closed-form for (28) and is approximately equal to $[\beta/(1-\beta)(B/B_v) - 1]^{-1}$ when $\beta \approx 1$.

The results from evaluating the CRBs for several scenarios are shown in Figure 5. In the plots, the CRB based on (25) is indicated by the solid line for $\Omega \in [0, 1]$, while the Schultheiss/Weinstein (S-W) CRBs for $\Omega = 0$ and $\Omega = 1$ in (26) and (27) are indicated by $*$. Figure 5(a) shows the CRB variation with saturation Ω and scattered signal bandwidth B_v. (The values of all parameters are specified in the caption to Figure 5.) The CRB with no scattering ($\Omega = 0$) is independent of B_v and agrees with the S-W formula in (26). With full scattering ($\Omega = 1$), the CRB agrees with the S-W approximation in (27) when $B_v T > 1$. Note that the CRB increases rapidly for small values of $\Omega > 0$, and then the variation is fairly flat with Ω. Figure 5(b) shows the CRB variation with saturation Ω and observation time T. Again we see the agreement with the S-W formula in (26) for all values of T and (27) for $B_v T > 1$, and the rapid increase in the CRB for small values of $\Omega > 0$. Figure 5(c) shows the CRB variation with saturation Ω and average SNR. Note that the CRB is fairly insensitive to SNR for $\Omega > 0$ and inversely proportional to SNR with no scattering ($\Omega = 0$). The SNR floor in the CRB is caused by the randomness of the scattered signal component. The S-W formula in (27) gives the high-SNR limit for large $B_v T$, and Figure 5(c) shows that (27) is reasonably accurate even for the case $B_v T = 1$ when the SNR > 10 dB. For parameter values that are commonly encountered in aeroacoustics, e.g., $B_v = 0.1$ Hz, $T = 1$ sec, and SNR $= 30$ dB, Figure 5 indicates that scattering increases the $\sqrt{\mathrm{CRB}}$ by about a factor of 10.

3.2 Doppler frequency estimation with scattered signals

Estimators for f_d based on the model (21) are considered in this subsection. We do not consider the general case in which the saturation $\Omega \in [0, 1]$ is unknown. Instead, we consider the maximum-

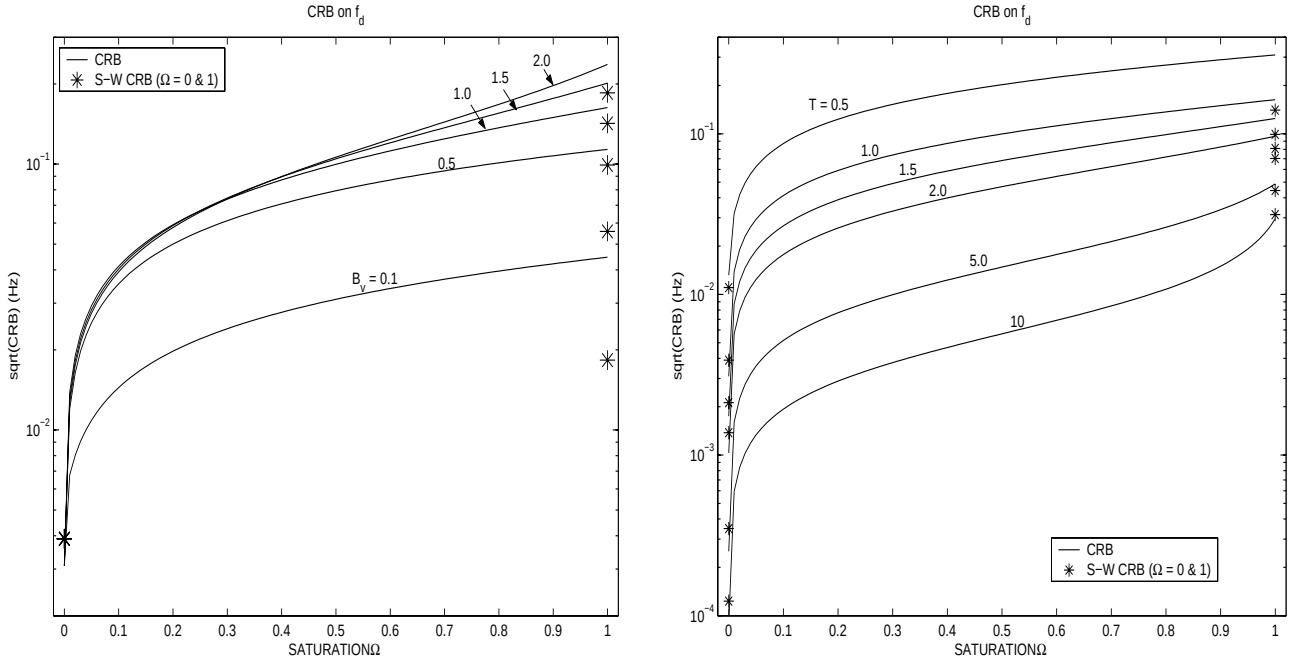

(a)

(b)

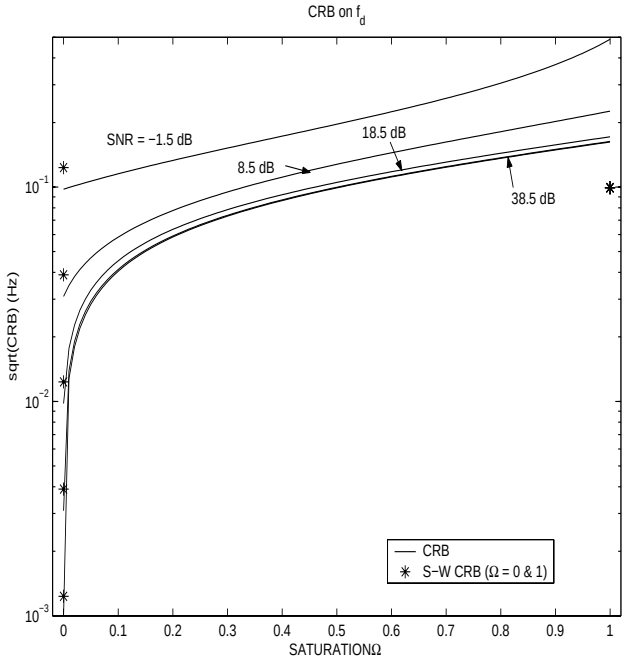

(c)

Figure 5: CRBs for estimation of f_d with various saturation Ω, scattered signal bandwidth B_v, observation time T, and SNR. The Doppler shift value is $f_d = -0.2$ Hz. (a) SNR = 28.5 dB, $B = 7$ Hz, $T = 1$ sec, and B_v from 0.1 to 2.0 Hz. (b) SNR = 28.5 dB, $B = 7$ Hz, $B_v = 1$ Hz, and T from 0.5 to 10.0 sec. (c) $B = 7$ Hz, $B_v = 1$ Hz, and $T = 1$ sec, and SNR from -1.5 to 38.5 dB.

likelihood (ML) estimator for the case of no scattering ($\Omega = 0$) and an estimator that was proposed by Besson and Stoica [21] for the case of full scattering ($\Omega = 1$). The periodogram (P-GRAM) is the ML estimator with no scattering, and is given by

$$\text{P-GRAM:} \quad \widehat{f}_d = \underset{f_d}{\text{argmax}} \left| \sum_{n=0}^{N-1} \widetilde{z}(nT_s) \, \exp(j2\pi f_d \, nTs) \right|^2 \tag{30}$$

where $T_s = 1/B$. The P-GRAM exploits the known form of the deterministic signal component.

For the case of full scattering ($\Omega = 1$), the signal component in (21) is a random process with unknown covariance matrix $\mathbf{R}_{\tilde{v}}$ (or, equivalently, unknown PSD shape $G_{\tilde{v}}(f)$). The unknown covariance matrix $\mathbf{R}_{\tilde{v}}$ complicates the estimation of f_d. If $\mathbf{R}_{\tilde{v}}$ is real-valued and Toeplitz, which agrees with our model, Besson and Stoica [21] proposed the following estimator for f_d that accounts for the unknown $\mathbf{R}_{\tilde{v}}$:

$$\text{C}^2\text{-GRAM:} \quad \widehat{f}_d = \underset{f_d}{\text{argmax}} \ \text{Re} \left\{ \sum_{m=1}^{N-1} \widehat{r}_{\tilde{z}}[m]^2 \, \exp(j4\pi f_d \, mTs) \right\}, \tag{31}$$

where $\widehat{r}_{\tilde{z}}[m]$ is a consistent estimate of the m^{th} lag of the sensor signal autocorrelation,

$$\widehat{r}_{\tilde{z}}[m] = \frac{1}{N-m} \sum_{n=m}^{N-1} \widetilde{z}(nT_s) \, \widetilde{z}((n-m)T_s)^*. \tag{32}$$

The estimator in (31) is labeled C^2-GRAM because it is similar to the correlogram (C-GRAM) except that the correlation estimates are squared to compensate for the unknown $\mathbf{R}_{\tilde{v}}$. Note that the summations in (30) and (31) can both be evaluated efficiently using the (inverse) FFT.

Figure 6 contains simulated mean-squared error (MSE) results for both estimators for the range of saturation values $\Omega \in [0, 1]$. The processing bandwidth is $B = 5$ Hz, the observation time is $T = 2$ sec, the Doppler shift is $f_d = 0.31$ Hz, and the MSE results are based on $10,000$ runs for each case. Figures 6(a) and (b) have average SNR = 30 dB, while Figures 6(c) and (d) have average SNR = 10 dB. Figures 6(a) and (c) have scattering bandwidth $B_v = 1$ Hz, while Figures 6(b) and (d) have scattering bandwidth $B_v = 0.1$ Hz. The P-GRAM and C^2-GRAM estimators perform similarly for the conditions in these simulations. The MSEs of both estimators are close to the CRB for $\Omega < 0.1$, then the MSE diverges from the CRB for larger values of Ω. For $\Omega > 0.5$, the MSEs are fairly insensitive to the SNR and B_v values.

4 Examples

Two examples are presented in this section. First we consider Doppler estimation for a harmonic source at various ranges using the model for saturation in (23) and (24). Then we present an example of differential Doppler estimation based on measured aeroacoustic data from a ground vehicle.

4.1 Doppler estimation for a harmonic source

Let us consider a harmonic source with fundamental frequency 15 Hz, and suppose that harmonics 3, 6, 9, and 12 (at 45, 90, 135, and 180 Hz) are used for Doppler estimation. According to the model for saturation Ω in (23), (24), and Figure 3(b), Ω varies with frequency and range. The

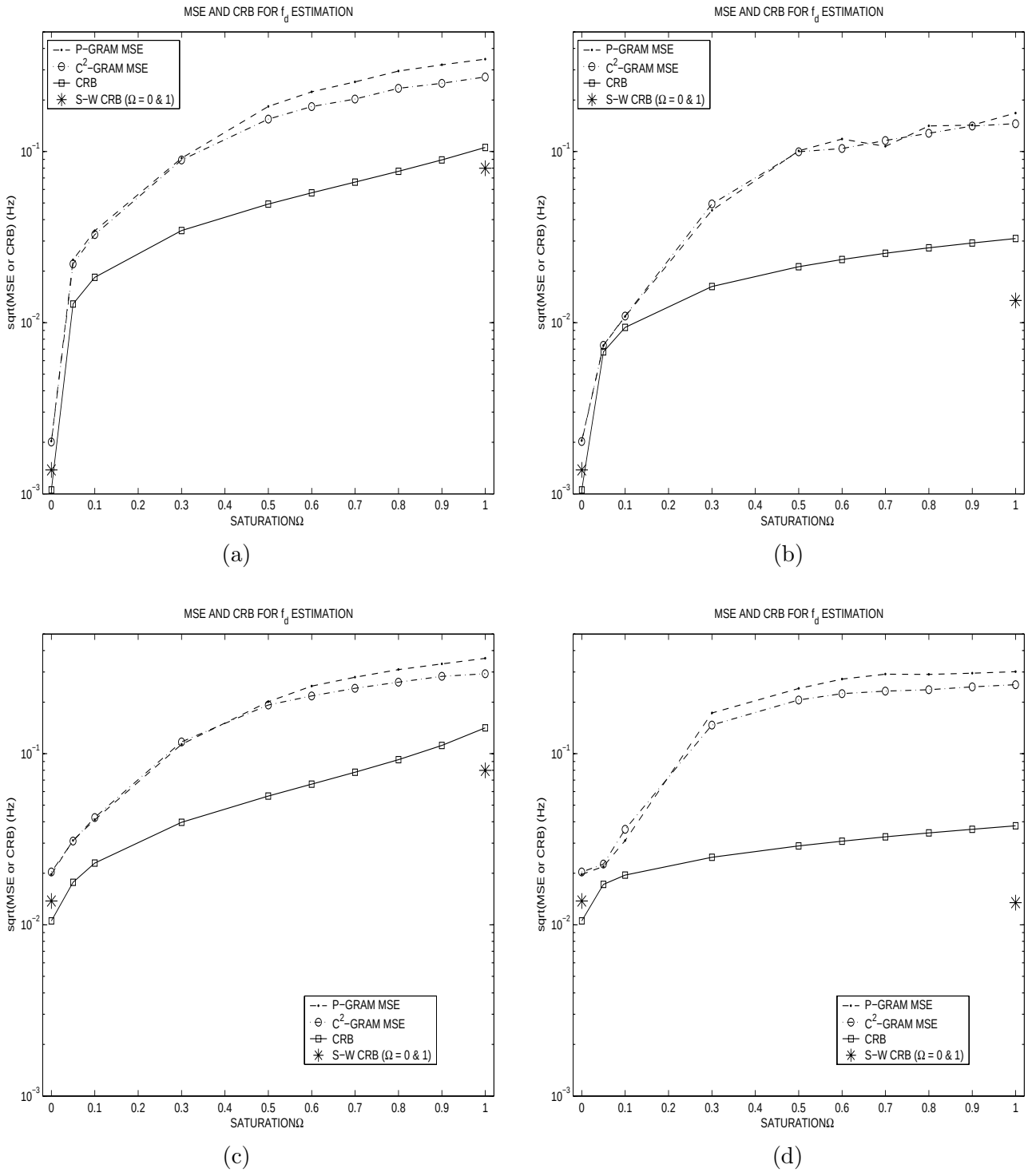

Figure 6: Comparison of frequency estimation mean-squared error (MSE) with the CRB for $B = 5$ Hz, $T = 2$ sec, and $f_d = 0.31$ Hz based on 10,000 runs for each case. (a) Average SNR = 30 dB, $B_v = 1$ Hz. (b) Average SNR = 30 dB, $B_v = 0.1$ Hz. (c) Average SNR = 10 dB, $B_v = 1$ Hz. (d) Average SNR = 10 dB, $B_v = 0.1$ Hz.

Freq. (Hz)	Range (m)						
	5	10	20	40	80	160	320
45	0.004	0.008	0.016	0.032	0.063	0.122	0.230
90	0.016	0.032	0.063	0.122	0.230	0.409	0.648
135	0.036	0.071	0.137	0.255	0.444	0.691	0.905
180	0.063	0.122	0.230	0.407	0.648	0.876	0.985

Table 1: Values of saturation Ω for harmonic frequencies at various ranges under mostly sunny conditions using (23) and (24).

Freq. (Hz)	Range (m)						
	5	10	20	40	80	160	320
45	0.004	0.006	0.008	0.013	0.019	0.031	0.053
90	0.007	0.010	0.015	0.023	0.034	0.054	0.096
135	0.011	0.015	0.022	0.032	0.049	0.078	0.145
180	0.014	0.020	0.028	0.041	0.061	0.097	0.171

Table 2: $\sqrt{\text{CRB}}$ on Doppler frequency shift for harmonic frequencies at various ranges for the saturation values in Table 1.

saturation values for ranges from 5 to 320 m are shown in Table 1, where Ω varies over much of the range from 0 to 1. The CRB on Doppler estimation will be different for each harmonic frequency, depending on the range of the source.

We consider a processing bandwidth $B = 10$ Hz, observation time $T = 2$ sec, and scattering bandwidth $B_v = 0.5$ Hz. The source range is varied from 5 m to 320 m, and the SNR is proportional to $1/\text{range}^2$, resulting in SNR variations from 33 dB at range 5 m to -3 dB at range 320 m. Table 2 contains the $\sqrt{\text{CRB}}$ on Doppler frequency estimation for each frequency and range. The $\sqrt{\text{CRB}}$ on Doppler estimation is smaller at the 45 Hz harmonic than the 180 Hz harmonic by about a factor of 3 at each range. The $\sqrt{\text{CRB}}$ gets larger by about an order of magnitude when the source range increases from 10 m to 320 m.

4.2 Example with measured data

An example using measured aeroacoustic data [9] is shown in Figure 7, where Figure 7(a) shows the path of a tracked vehicle. Figure 7(b) shows the estimated differential Doppler shift of a frequency component near 38 Hz at sensor arrays 1 and 3 during the 10 sec time segment indicated in Figure 7(a). Note from the MEAN ESTIMATE line in Figure 7(b) that smoothing the Doppler estimates over time provides an error from GPS ground truth that is comparable to $\sqrt{\text{CRB}} \approx 0.1$ Hz, where the CRB is computed for conditions that approximate those in the experiment.

5 Concluding Remarks

We have developed a model for the Doppler frequency shift at acoustic sensors that includes the effects of scattering by atmospheric turbulence. CRBs and algorithms for Doppler frequency estimation were presented. It will be useful to extend the results to obtain CRBs on source localization accuracy using differential Doppler with multiple sensors. In addition, it will be useful to evaluate

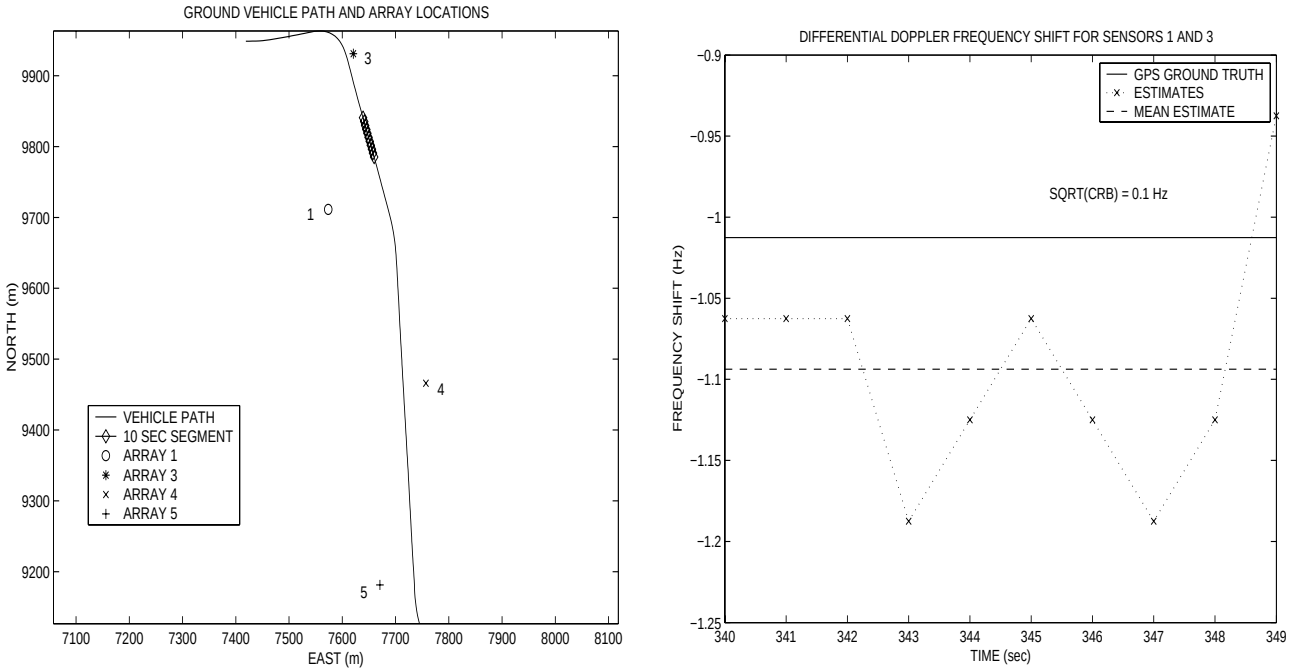

(a) (b)

Figure 7: (a) Vehicle path and array locations. (b) Differential Doppler estimates using sensors 1 and 3 during a 10-second segment.

the relative accuracy of source localization based on triangulation of bearings with triangulation based on differential Doppler.

Acknowledgment

The authors thank Dr. D. Keith Wilson for helping the authors to formulate and understand the scattering models.

References

[1] D.K. Wilson, "Performance bounds for acoustic direction-of-arrival arrays operating in atmospheric turbulence," *J. Acoust. Soc. Am.*, vol. 103, no. 3, pp. 1306-1319, March 1998.

[2] S.L Collier and D.K. Wilson, "Performance bounds for passive arrays operating in a turbulent medium: Plane-wave analysis," *J. Acoust. Soc. Am.*, Vol. 113, No. 5, pp. 2704–2718, May 2003.

[3] S.L Collier and D.K. Wilson, "Performance bounds for passive sensor arrays operating in a turbulent medium II: Spherical-wave analysis," in review at *J. Acoust. Soc. Am.*, June 2003.

[4] D.K. Wilson, "A turbulence spectral model for sound propagation in the atmosphere that incorporates shear and buoyancy forcings", *J. Acoust. Soc. Am.*, **108** (5), Pt. 1, pp. 2021–2038, Nov. 2000.

[5] V. E. Ostashev and D. K. Wilson, "Relative contributions from temperature and wind velocity fluctuations to the statistical moments of a sound field in a turbulent atmosphere," *Acta Acustica*, vol. 86, pp. 260–268, 2000.

[6] D.K. Wilson, B.M. Sadler, T. Pham, "Simulation of detection and beamforming with acoustical ground sensors," *Proc. SPIE 2002 AeroSense Symp.*, pp. 50–61, Orlando, FL, April 1-5, 2002.

[7] D. E. Norris, D. K. Wilson, and D. W. Thomson, "Atmospheric scattering for varying degrees of saturation and turbulent intermittency," *J. Acoust. Soc. Am.*, vol. 109, pp. 1871–1880, 2001.

[8] R.J. Kozick, B.M. Sadler, and D.K. Wilson, "Signal Processing and Propagation for Aeroacoustic Sensor Networking," to appear in *Frontiers in Distributed Sensor Networks*, S.S. Iyengar and R.R. Brooks (Eds.), CRC Press, 2004.

[9] R.J. Kozick and B.M. Sadler, "Source localization with distributed sensor arrays and partial spatial coherence," to appear in *IEEE Trans. on Signal Processing*, 2003.

[10] P.M. Schultheiss and E. Weinstein, "Estimation of differential Doppler shifts," *J. Acoust. Soc. Am.*, vol. 66, no. 5, pp. 1412-1419, Nov. 1979.

[11] R.J. Kozick and B.M. Sadler, "Tracking Moving Acoustic Sources with a Network of Sensors," Army Research Laboratory Technical Report ARL-TR-2750, October 2002.

[12] H.E. Bass, R. Raspet, and J.O. Messer, "Experimental determination of wind speed and direction using a three microphone array," *J. Acoust. Soc. Am.*, Vol. 97, pp. 695–696, 1995.

[13] T. F. W. Embleton, "Tutorial on sound propagation outdoors," *J. Acoust. Soc. Am.*, vol. 100, pp. 31–48, 1996.

[14] E. M. Salomons, *Computational Atmospheric Acoustics* (Kluwer, Dordrecht, 2001).

[15] G. A. Daigle, J. E. Piercy, and T. F. W. Embleton, "Line-of-sight propagation through atmospheric turbulence near the ground," *J. Acoust. Soc. Am.*, vol. 74, pp. 1505–1513, 1983.

[16] H. E. Bass, L. N. Bolen, R. Raspet, W. McBride, and J. Noble, "Acoustic propagation through a turbulent atmosphere: experimental characterization," *J. Acoust. Soc. Am.*, vol. 90, pp. 3307–3313, 1991.

[17] D.E. Norris, D.K. Wilson, D.W. Thomson, "Correlations between acoustic travel-time fluctuations and turbulence in the atmospheric surface layer," *Acta Acustica*, vol. 87, pp. 677–684, 2001.

[18] D.K. Wilson, J.M. Noble, M.A. Coleman, "An experimental study of sound propagation in the nighttime atmosphere," *Proc. 2002 Meeting of the MSS Specialty Group on Battlefield Acoustic and Seismic Sensing*, Sept. 24-26, 2002.

[19] R.J. Kozick and B.M. Sadler, "Information sharing between localization, tracking, and identification algorithms," *Proc. 2002 Meeting of the MSS Specialty Group on Battlefield Acoustics and Seismics*, Laurel, MD, Sept. 24–27, 2002.

[20] S.M. Kay, *Fundamentals of Statistical Signal Processing: Estimation Theory*, Prentice-Hall, 1993.

[21] O. Besson and P. Stoica, "On frequency offset estimation for flat-fading channels," *IEEE Communications Letters*, vol. 5, no. 10, pp. 402–404, Oct. 2001.